# Comprehensive multiwavelength modelling of the afterglow of GRB 050525A

L. Resmi, K. Misra, G. Jóhannesson, A. J. Castro Tirado, J. Gorosabel, M. Jelínek, D. Bhattacharya, P. Kubánek, G. C. Anupama, A. Sota, et al.

Monthly Notices of the ROYAL ASTRONOMICAL SOCIETY

Mon. Not. R. Astron. Soc. **427,** 288–297 (2012) doi:10.1111/j.1365-2966.2012.21713.x

# Comprehensive multiwavelength modelling of the afterglow of GRB 050525A

L. Resmi,[1,2⋆] K. Misra,[3,4] G. Jóhannesson,[5] A. J. Castro-Tirado,[6] J. Gorosabel,[6] M. Jelínek,[6] D. Bhattacharya,[4] P. Kubánek,[6] G. C. Anupama,[7] A. Sota,[6] D. K. Sahu,[7] A. de Ugarte Postigo,[8] S. B. Pandey,[9] R. Sánchez-Ramírez,[6] M. Bremer[10] and R. Sagar[9]

[1]*Tata Institute of Fundamental Research, Mumbai 400 005, India*
[2]*Institut d'Astrophysique de Paris, Paris 75014, France*
[3]*Space Telescope Science Institute, Baltimore, MD 21218, USA*
[4]*Inter University Center for Astronomy and Astrophysics, Post Bag 4, Ganeshkhind, Pune 411 007, India*
[5]*Science Institute, University of Iceland, Dunhaga 3, IS-107 Reykjavik, Iceland*
[6]*Instituto de Astrofísica de Andalucía (IAA-CSIC), PO Box 03004, 18080 Granada, Spain*
[7]*Indian Institute of Astrophysics, Koramangala, Bangalore 560 034, India*
[8]*Dark Cosmology Center, Niels Bohr Institute, Juliane Maries Vej 30, Copenhagen 2100, Denmark*
[9]*Aryabhatta Research Institute of Observational Sciences, Manora Peak, Nainital 263 129, India*
[10]*Institute de Radioastronomie Millimétrique (IRAM), 300 rue de la Piscine, 38406 Saint Martin Hères, France*

Accepted 2012 July 11. Received 2012 July 11; in original form 2011 July 12

## ABSTRACT

The *Swift* era has posed a challenge to the standard blast-wave model of gamma-ray burst (GRB) afterglows. The key observational features expected within the model are rarely observed, such as the achromatic steepening ('jet break') of light curves. The observed afterglow light curves showcase additional complex features requiring modifications within the standard model. Here we present optical/near-infrared observations, millimetre upper limits and comprehensive broad-band modelling of the afterglow of the bright GRB 0505025A, detected by *Swift*. This afterglow cannot be explained by the simplistic form of the standard blast-wave model. We attempt modelling multiwavelength light curves using (i) a forward–reverse shock model, (ii) a two-component outflow model and (iii) a blast-wave model with a wind termination shock. The forward–reverse shock model cannot explain the evolution of the afterglow. The two-component model is able to explain the average behaviour of the afterglow very well but cannot reproduce the fluctuations in the early X-ray light curve. The wind termination shock model reproduces the early light curves well but deviates from the global behaviour of the late-time afterglow.

**Key words:** techniques: photometric – gamma-ray burst: individual: GRB 050525A.

## 1 INTRODUCTION

Gamma-ray bursts (GRBs) are extremely energetic cosmic explosions which outshine the entire gamma-ray sky for a few seconds. The launch of *Swift* (Gehrels et al. 2004), a dedicated satellite to detect GRBs and rapidly follow up their afterglow emission, has revolutionized the study of the most energetic cosmic explosions in the Universe.

In the standard blast-wave model for GRB afterglows (Rees & Meszaros 1992; Paczynski & Rhoads 1993; also see Piran 1999 for a review), a relativistic shock decelerates through a uniform circumburst medium, heats up the matter, accelerates particles and enhances the magnetic field downstream. Synchrotron radiation from the shocked particles is observed as the afterglow. The snapshot synchrotron spectrum can be characterized by four spectral parameters (apart from the electron index $p$): the injection frequency $\nu_{\rm m}$, the cooling frequency $\nu_{\rm c}$, the self-absorption frequency $\nu_{\rm a}$ and the peak flux $f_{\rm m}$. The spectral parameters can be mapped to four physical parameters: the isotropic equivalent energy $E_{\rm iso}$, the ambient medium density (parametrized as the number density $n_0$ for a constant density medium and as $A_\star$ for a wind-driven medium for which $\rho(r) = 5.5 \times 10^{11} \frac{A_\star}{\rm g\,cm^{-1}} \left(\frac{r}{\rm cm}\right)^{-2}$ as in Chevalier & Li 1999), and the fractional energy content in non-thermal electrons and magnetic

⋆E-mail: resmi@tifr.res.in

field ($\epsilon_e$ and $\epsilon_B$, respectively). Jet break, a simultaneous steepening seen in the multifrequency light curves considered as a signature of the collimated outflow from the burst (Rhoads 1999), if observed (at time $t_j$ since burst), gives a handle on the initial collimation angle ($\theta_j$) of the explosion, and hence on the total kinetic energy involved ($E_{tot}$).

The model was largely successful in explaining the pre-*Swift* observations of GRB afterglows. However, *Swift* with its ability to locate the afterglow within minutes of the burst and follow it up in ultraviolet (UV), optical and X-ray bands has revealed complexity in the early afterglow emission that is not predicted by the model. The X-ray light curves in the *Swift* era have been rather dramatic, with steep decays, plateaus and flares, not witnessed earlier (Nousek et al. 2006; Chincarini et al. 2007). Moreover, in several afterglows, flux evolution did not follow the predicted spectral–temporal relations (Liang et al. 2008). This has led to the conclusion that afterglow light curves differ drastically from burst to burst, owing to various physical processes shaping the flux evolution in various bands (Zhang et al. 2006). Another open issue in the *Swift* era is the absence of a jet break. These complications often make it a demanding task to extract the physics of the burst and its surroundings from afterglow data.

The bright low redshift ($z = 0.606$; Foley et al. 2005) GRB 050525A was detected by the *Swift*-Burst Alert Telescope (BAT) on 2005 May 25 at 00:02:53 UT (Band et al. 2005). We refer to the burst trigger time as $t_0$. An isotropic equivalent gamma-ray energy of $2.3 \times 10^{52}$ erg is inferred for the observed BAT fluence at a distance of 3.57 Gpc (assuming $\Omega_m = 0.3$, $\Omega_\Lambda = 0.7$ and $H_0 = 70\,\mathrm{km\,s^{-1}\,Mpc^{-1}}$). The Ultraviolet Optical Telescope (UVOT) *V*-band observations started at $T = t - t_0 \sim 65$ s and X-ray Telescope (XRT) observations began at $T \sim 75$ s leading to well-sampled early afterglow light curves. The proximity of the burst and the brightness of the afterglow made it a very good target for multiwavelength observations. Ground-based optical observations including robotic telescopes (Klotz et al. 2005; Della Valle et al. 2006), radio observations in multiple frequencies by the Very Large Array (VLA; Cameron & Frail 2005) and *Spitzer* observations at ∼2 d in multiple infrared (IR) bands (Heng et al. 2008) have been reported in the literature. However, detailed modelling involving the full evolution of the relativistic shock to infer the physical parameters has not been attempted for this burst.

In this paper, we present a new set of *VRIJH* observations using eight different optical telescopes and millimetre (mm) upper limits from the IRAM Plateau de Bure Interferometer (PdBI). We supplement our data with *Swift*-UVOT and XRT data reported by Blustin et al. (2006), the optical data reported by Klotz et al. (2005) and Della Valle et al. (2006) and the radio data from the VLA afterglow repository[1] to study the broad-band evolution of the afterglow. We model the afterglow using three different extensions of the standard blast-wave model e.g. the forward–reverse shock model (Mészáros & Rees 1999), the two-component model (Berger et al. 2003) and a model including a wind termination shock (Pe'er & Wijers 2006). Section 2 gives a description of the data acquired from different telescopes and the analysis techniques. Multiwavelength modelling under various premises is described in Section 3. Section 4 provides a summary of the multiwavelength modelling results.

[1] http://www.aoc.nrao.edu/~dfrail/allgrb_table.shtml

## 2 DATA ACQUISITION AND REDUCTION

### 2.1 Millimetre wave observations

The IRAM PdBI, France (Guilloteau et al. 1992), observed the position of GRB 050525A simultaneously at 92.682 and 214.712 GHz about 1 d after the burst (see Table 1). The fields of view of the 15-m antennas at these frequencies are respectively 54.3 and 23.5 arcsec, and the synthesized beams in the compact five-antenna configuration are 7.05 arcsec × 5.58 arcsec at $PA = 74^\circ$ and 3.10 arcsec × 2.36 arcsec at $PA = 78^\circ$ where the position angle *PA* of the major beam axis is defined from North over East. The data reduction was done with the GILDAS[2] software. We performed point source fits in the UV plane; for a fit fixed to the phase centre position, a signal of at least $3\sigma$ is needed to claim a detection, whereas a point source elsewhere in the field of view must have at least $5\sigma$. We did not detect a mm counterpart, neither on the phase centre coordinates nor elsewhere in the field of view. In the following, we take the $3\sigma$ levels as upper limits, i.e. 1.02 mJy for 92.682 GHz and 3.66 mJy for 214.712 GHz (Table 1).

### 2.2 Optical and near-IR observations of the afterglow

The afterglow of GRB 050525A was observed using different optical facilities in the broad-bands *VRIJH* during 2005 May 25 to July 01. We used the 0.2-m BOOTES1-B telescope located at the INTA-CEDEA station at El Arenosillo, Huelva, Spain; the 1.04-m Sampurnanand Telescope (ST) in India; the 1.2-m semirobotic Mercator telescope at La Palma; the 1.5-m telescope at the Observatorio de Sierra Nevada (OSN); the 2.01-m Himalayan Chandra Telescope (HCT) in India; the 2.5-m Isaac Newton Telescope (INT) and the 2.2-m and 3.5-m telescopes at the Calar Alto Observatory (CAHA) for the observations (Table 2). Several bias and twilight flat frames were acquired from different telescopes for pre-processing the CCD images. The pre-processing was done in a standard fashion including bias subtraction, flat fielding and cosmic ray removal in all object frames. Standard data reduction software packages (IRAF,[3] MIDAS[4] and DAOPHOT[5]; Stetson 1987) were used for photometric analysis. The instrumental magnitudes of the optical afterglow were differentially calibrated using nearby secondary stars from the list of Henden (2005). A full compilation of *VRIJH* magnitudes of the afterglow is presented in Table 2.

The earliest observations were taken with the BOOTES1-B telescope at $T \sim 0.0044$ d. We detect the afterglow in a co-added early-time BOOTES1-B image. Fig. 1 shows the optical afterglow in the early-time BOOTES1-B image and in an image taken ∼2 d after the burst with the OSN telescope. Late-time observations of the afterglow on 2005 June 30 and July 01 with the 2.2-m CAHA and the 2.5-m INT, respectively, resulted in a non-detection and an upper limit.

In Fig. 2, we show the optical/near-IR (NIR) and mm data presented in this paper along with the published data in X-ray, optical and radio frequencies. We present an *I*-band light curve

[2] http://www.iram.fr/IRAMFR/GILDAS

[3] IRAF stands for Image Reduction and Analysis Facility distributed by the National Optical Astronomy Observatories which is operated by the Association of Universities for Research in Astronomy, Inc. under cooperative agreement with the National Science Foundation.

[4] MIDAS stands for Munich Image and Data Analysis System designed and developed by the European Southern Observatory ESO in Munich, Germany.

[5] DAOPHOT stands for Dominion Astrophysical Observatory Photometry.

**Table 1.** Log of mm wave observations.

| Date-obs (UT) (d) | Time since burst ($T$)[a] (d) | Frequency (GHz) | $3\sigma$ upper limit (mJy) | Synthesized beam (arcsec$^2$) | Position angle (deg) |
|---|---|---|---|---|---|
| 2005-05-25.9188–26.3479 | 0.9168–1.3459 | 92.682 | <1.02 | 7.05 × 5.58 | 74 |
| | | 214.712 | <3.66 | 3.10 × 2.36 | 78 |

[a] $T = t - t_0$ where $t_0 = 25\text{-}05\text{-}25.002$ d.

**Table 2.** Log of optical and NIR observations.

| Date-obs (UT) (d) | Time since burst ($T$)[a] (d) | Magnitude (mag) | Exp time (s) | Filter | Telescope |
|---|---|---|---|---|---|
| 2005-05-25.0101 | 0.0081 | 16.510 ± 0.390 | 10 × 32 | *V* | 0.2-m Bootes1-B |
| 2005-05-25.0682 | 0.0680 | 17.500 ± 0.165 | 300 | *V* | 1.2-m Mercator |
| 2005-05-25.0955 | 0.0953 | 18.260 ± 0.134 | 300 | *V* | 1.2-m Mercator |
| 2005-05-25.1046 | 0.1044 | 18.253 ± 0.072 | 300 | *V* | 1.2-m Mercator |
| 2005-05-25.1347 | 0.1344 | 18.517 ± 0.082 | 300 | *V* | 1.2-m Mercator |
| 2005-05-25.1528 | 0.1526 | 19.107 ± 0.293 | 300 | *V* | 1.2-m Mercator |
| 2005-05-25.1619 | 0.1616 | 19.063 ± 0.142 | 300 | *V* | 1.2-m Mercator |
| 2005-05-25.1713 | 0.1711 | 18.941 ± 0.090 | 300 | *V* | 1.2-m Mercator |
| 2005-05-25.1940 | 0.1937 | 18.878 ± 0.128 | 300 | *V* | 1.2-m Mercator |
| 2005-07-01.0386 | 37.0366 | >22.5 | 1000 × 5 | V | 2.5-m INT |
| 2005-05-25.1092 | 0.1089 | 17.790 ± 0.054 | 300 | *R* | 1.2-m Mercator |
| 2005-05-25.1137 | 0.1169 | 17.969 ± 0.043 | 900 | *R* | 1.2-m Mercator |
| 2005-05-25.7800 | 0.7822 | 20.860 ± 0.079 | 720 | *R* | 2.0-m HCT |
| 2005-05-25.8108 | 0.8123 | 20.819 ± 0.070 | 600 | *R* | 2.0-m HCT |
| 2005-05-25.8376 | 0.8426 | 20.850 ± 0.079 | 1200 | *R* | 2.0-m HCT |
| 2005-05-25.9111 | 0.9143 | 21.370 ± 0.270 | 900 | *R* | 1.0-m ST |
| 2005-05-25.9130 | 0.9144 | 21.399 ± 0.230 | 600 | *R* | 2.0-m HCT |
| 2011-05-26.1508–30.0955 | 2131.1488–2135.0935 | >24.3 | 18 × 900 | *r* | 2.2-m CAHA |
| 2005-05-25.0485 | 0.0483 | 16.533 ± 0.093 | 300 | *I* | 1.2-m Mercator |
| 2005-05-25.0544 | 0.0541 | 16.517 ± 0.097 | 300 | *I* | 1.2-m Mercator |
| 2005-05-25.0594 | 0.0591 | 16.656 ± 0.043 | 300 | *I* | 1.2-m Mercator |
| 2005-05-25.0638 | 0.0636 | 16.547 ± 0.056 | 300 | *I* | 1.2-m Mercator |
| 2005-05-25.0910 | 0.0907 | 17.249 ± 0.098 | 300 | *I* | 1.2-m Mercator |
| 2005-05-25.1001 | 0.0998 | 17.247 ± 0.043 | 300 | *I* | 1.2-m Mercator |
| 2005-05-25.1301 | 0.1299 | 17.643 ± 0.054 | 300 | *I* | 1.2-m Mercator |
| 2005-05-25.1574 | 0.1571 | 17.726 ± 0.159 | 300 | *I* | 1.2-m Mercator |
| 2005-05-25.1758 | 0.1756 | 18.002 ± 0.098 | 300 | *I* | 1.2-m Mercator |
| 2005-05-25.1849 | 0.1847 | 18.024 ± 0.090 | 300 | *I* | 1.2-m Mercator |
| 2005-05-25.5918 | 0.5915 | 19.520 ± 0.119 | 300 | *I* | 1.0-m ST |
| 2005-05-25.6002 | 0.5999 | 19.200 ± 0.059 | 300 | *I* | 1.0-m ST |
| 2005-05-25.7826 | 0.7842 | 20.260 ± 0.100 | 630 | *I* | 2.0-m HCT |
| 2005-05-25.8216 | 0.8241 | 20.530 ± 0.070 | 780 | *I* | 2.0-m HCT |
| 2005-05-25.8514 | 0.8563 | 20.299 ± 0.100 | 1200 | *I* | 2.0-m HCT |
| 2005-05-25.8959 | 0.9008 | 20.829 ± 0.119 | 1200 | *I* | 2.0-m HCT |
| 2005-05-25.8995 | 0.9028 | 20.559 ± 0.270 | 900 | *I* | 1.0-m ST |
| 2005-05-25.9659 | 0.9744 | 20.627 ± 0.129 | 1800 | *I* | 1.5-m OSN |
| 2005-05-25.9223 | 0.9256 | 20.739 ± 0.280 | 900 | *I* | 1.0-m ST |
| 2005-05-27.1116 | 2.1096 | 22.390 ± 0.540 | 200 × 12 | *I* | 1.5-m OSN |
| 2005-06-30.9721 | 36.048 | >23 | 450 × 30 | *I* | 2.2-m CAHA |
| 2011-05-28.9855–30.0955 | 2133.9845–2135.0935 | 25.1 ± 0.4 | 17 × 900 | *i* | 2.2-m CAHA |
| 2011-05-26.1508–30.0955 | 2131.1488–2135.0935 | >24.1 | 18 × 900 | *g* | 2.2-m CAHA |
| 2005-05-25.0953 | 0.0936 | 15.779 ± 0.068 | 60.240 | *H* | 3.5-m CAHA |
| 2005-05-25.0963 | 0.0946 | 15.611 ± 0.072 | 60.240 | *H* | 3.5-m CAHA |
| 2005-05-25.0973 | 0.0956 | 15.713 ± 0.064 | 60.240 | *H* | 3.5-m CAHA |
| 2005-05-25.0983 | 0.0966 | 16.024 ± 0.093 | 60.240 | *H* | 3.5-m CAHA |
| 2005-05-25.0992 | 0.0976 | 15.737 ± 0.067 | 60.240 | *H* | 3.5-m CAHA |
| 2005-05-25.0866 | 0.0847 | 16.263 ± 0.039 | 21.079 | *J* | 3.5-m CAHA |
| 2005-05-25.0881 | 0.0865 | 16.337 ± 0.034 | 60.240 | *J* | 3.5-m CAHA |

**Table 2** – *continued*

| Date-obs (UT) (d) | Time since burst ($T$)[a] (d) | Magnitude (mag) | Exp time (s) | Filter | Telescope |
|---|---|---|---|---|---|
| 2005-05-25.0891 | 0.0875 | $16.257 \pm 0.035$ | 60.240 | *J* | 3.5-m CAHA |
| 2005-05-25.0901 | 0.0884 | $16.294 \pm 0.034$ | 60.240 | *J* | 3.5-m CAHA |
| 2005-05-25.0911 | 0.0894 | $16.263 \pm 0.034$ | 60.240 | *J* | 3.5-m CAHA |
| 2005-05-25.0920 | 0.0904 | $16.271 \pm 0.034$ | 60.240 | *J* | 3.5-m CAHA |
| 2005-05-25.0931 | 0.0914 | $16.353 \pm 0.035$ | 60.240 | *J* | 3.5-m CAHA |
| 2011-07-18.0320–18.1150 | 2245.0301–2245.1131 | $23.58 \pm 0.225$[b] | $83 \times 60$ | *J* | 3.5-m CAHA |
| 2011-07-19.0502–19.1077 | 2246.0483–2246.1059 | – | $57 \times 60$ | *J* | 3.5-m CAHA |

[a] $T = t - t_0$ where $t_0 = 25\text{-}05\text{-}25.002$ d.
[b]The magnitude is the result of the combination of the *J*-band data taken on 2011 July 18 and 19.

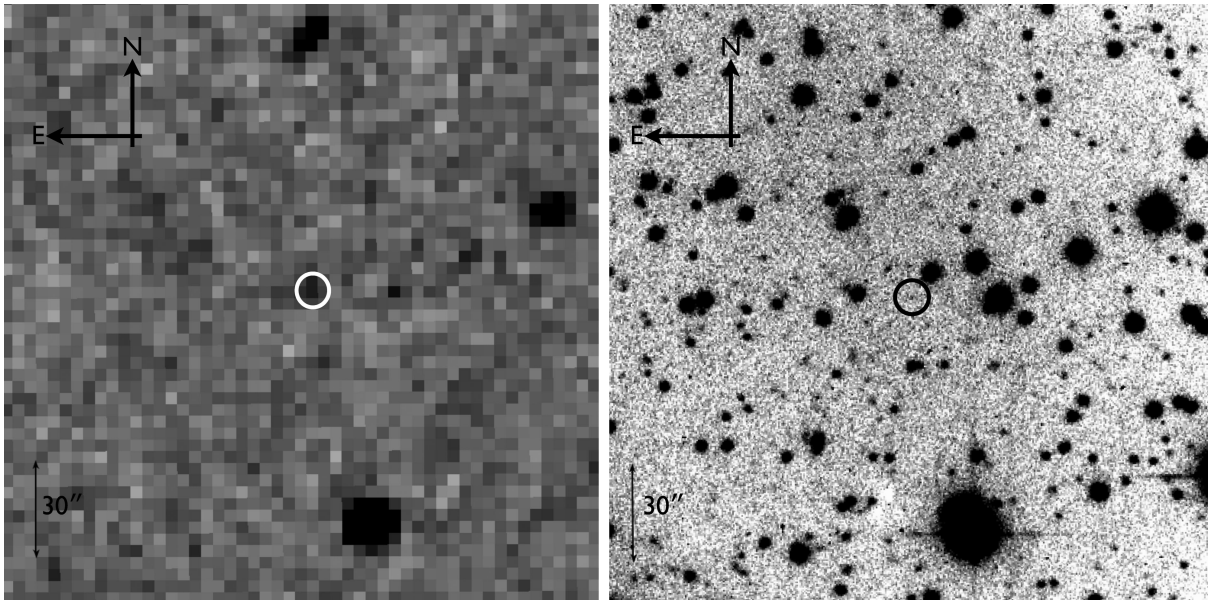


**Figure 1.** The GRB 050525A field. The left-hand image (at $T \sim 700$ s after the burst, *V* band) was taken with the 0.2-m BOOTES1-B telescope located at the INTA-CEDEA station at El Arenosillo, Huelva, Spain. The right-hand one, shown for comparison purposes, was taken at $T \sim 2$ d after the burst with the 1.5-m telescope at IAA-CSIC OSN in the *I* band. The circle is 5.0 arcsec in radius and indicates the location of the afterglow in the two images.

for this burst for the first time, which extends from $T \sim 0.05$ to 0.6 d, and our data fill the gap in the *V*-band light curve between 0.05 and 0.2 d ($T \sim 5800$–17 000 s). Our IR observations (*J* and *H* bands) are clustered around 0.09 d, but provide spectral information within the optical band that constrains model parameters.

### 2.3 Host galaxy observations

We obtained deep imaging of the GRB 050525A field in the *gri* bands between 2011 May 26 and 28 with the 2.2-m CAHA telescope. The data reduction was carried out in a manner similar to the one described in Section 2.2. A very faint source is detected in the *i* band at the location of the afterglow but only upper limits can be imposed in the *g* and *r* bands. The log of the observations is given in Table 2. We attempted further deep imaging in the *J* band on 2011 July 18–19 for a total exposure time of 2.33 h spread over two consecutive nights with the 3.5-m CAHA telescope equipped with the NIR camera $\text{Omega}_{2000}$. The photometric calibration is carried out by observing the UKIRT faint standards FS28 and FS30. We detect four faint sources close to the *Swift* XRT error circle in the *J*-band image. The source closest to the enhanced XRT position[6] and UVOT position reported in Blustin et al. (2006) is indicated in Fig. 3 and is assumed to be the host galaxy of GRB 050525A. The host galaxy photometry is presented in Table 2.

## 3 MULTIWAVELENGTH MODELLING RESULTS

GRB 050525A has a relatively well-sampled afterglow light curve (see Fig. 2). The *Swift* observations end at $T \sim 1$ d while ground-based *R*-band observations continue up to ∼20 d. The early X-ray light curve starts off with a power-law decay, but a minor flare is observed at $T \sim 0.0035$ d (Blustin et al. 2006). This flare is not seen in the optical light curves that undergo a smooth power-law decay. However, around $T \sim 0.02$ d, a re-brightening is observed in the *R*-band light curve. There is considerable scatter in the *R*-band light curve at this epoch, and unfortunately no other frequencies cover this epoch. The afterglow evolution after this period appears to be within the expectations of the standard blast-wave model with

[6] http://www.swift.ac.uk/xrt_positions/

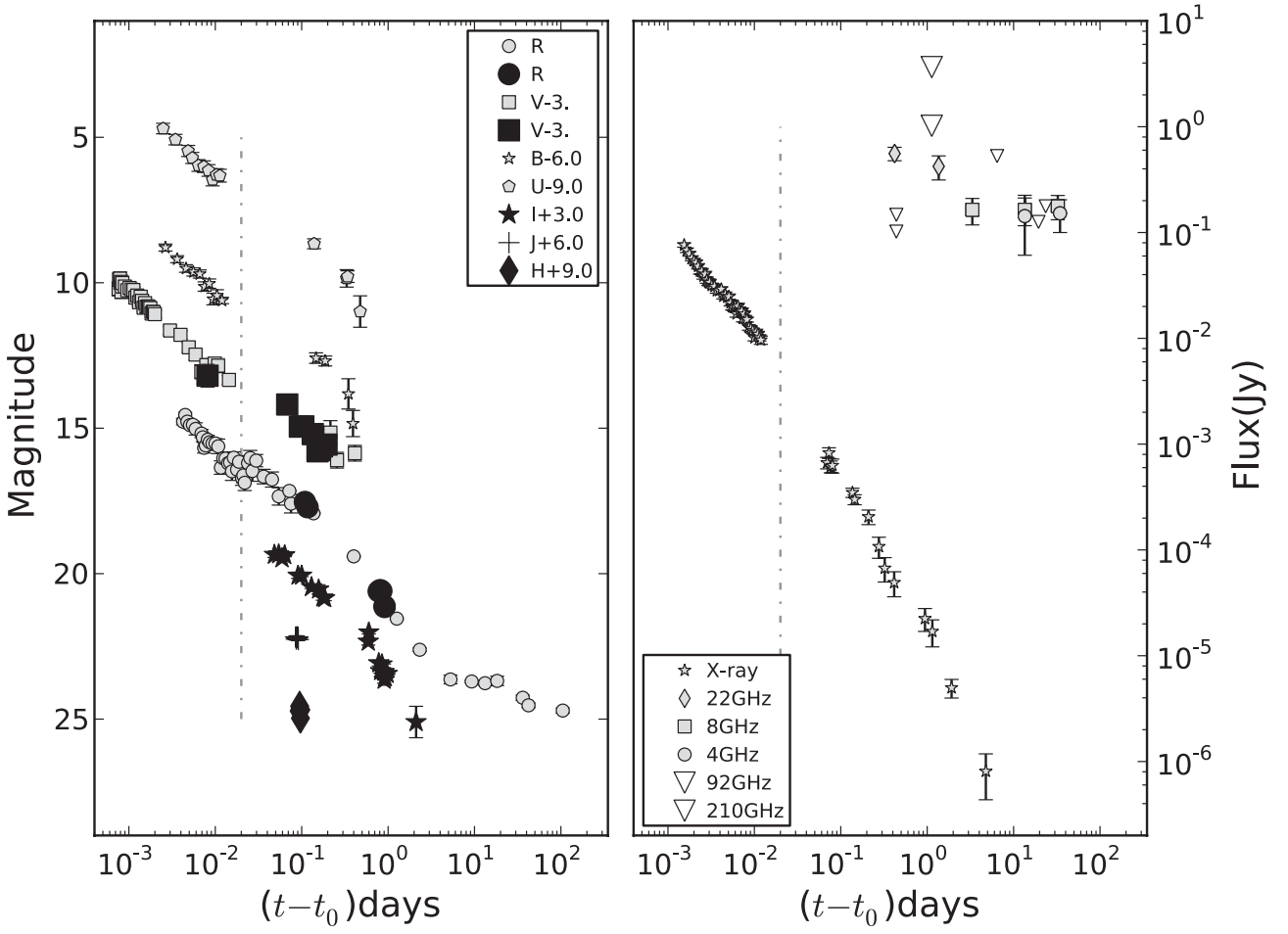


**Figure 2.** *UBVRIJH*, X-ray, radio and mm light curves of the afterglow of GRB 050525A. The dark- and light-coloured symbols correspond to the new data presented in this paper and the literature data, respectively. The upper limits, including the mm ones presented in this paper, are represented by open triangles. The dash–dotted vertical line corresponds to $T \sim 0.02$ d (see the text). The optical light curves are shifted arbitrarily for clarity.

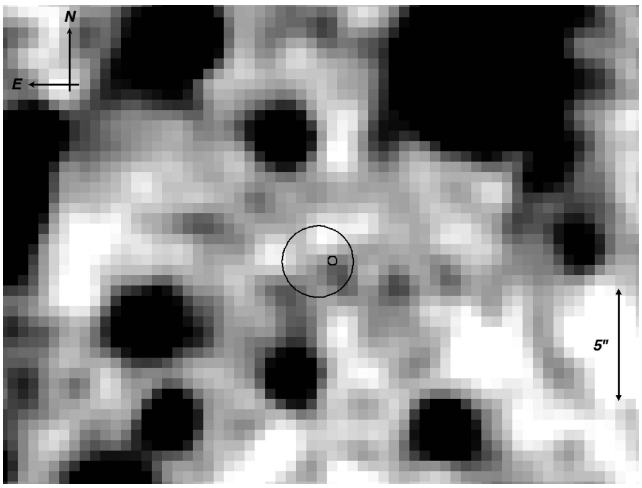


**Figure 3.** A late-time *J*-band image of the GRB 050525A field with the 3.5-m CAHA telescope. We detect four faint sources close to the *Swift* XRT error circle. The source closest to the enhanced XRT position (90 per cent error circle) and UVOT position ($1\sigma$ error circle) reported in Blustin et al. (2006) is indicated in the figure and is assumed to be the GRB host galaxy. The photometry of the host galaxy is presented in Table 2.

a near-simultaneous break and similar post-break indices in the optical and X-ray light curves (Blustin et al. 2006). However, the light curve before 0.02 d significantly deviates from the extrapolation of the power-law decay that is present afterwards. There is a change in the *R*-band light-curve normalization after this epoch, or in other words, an increase in the optical to X-ray spectral index with no colour evolution within the X-ray or optical bands. This suggests that the value of $\nu_c$ decreases rapidly in this period. A single component, like a forward shock (FS) emission, alone cannot explain the complete evolution of this afterglow. Either there are multiple emission components or there is a density discontinuity in the ambient medium.

We perform simultaneous multiwavelength fitting of the afterglow data to obtain the underlying physical parameters. Parametrized extinction laws for Milky Way (Cardelli, Clayton & Mathis 1989), Large Magellanic Cloud, Small Magellanic Cloud (Pei 1992) and starburst galaxy (Calzetti 1997) are used for modelling extinction due to the dust column in the host galaxy. A chi-square minimization procedure is used to derive the best-fitting parameters. For fitting we use all data except the late-time ($T > 5$ d) data in the *R* band that are possibly contaminated by a supernova (SN) component (see Section 3.4).

For the forward–reverse shock model and the two-component model, our code calculates the synchrotron flux $f_\nu(t)$ at an observed

frequency $\nu$ at a given time $t$ as a function of the four spectral parameters which evolve following the respective shock dynamics (Wijers & Galama 1999; Resmi & Bhattacharya 2008). We assume both wind-driven and constant density ambient medium while searching for the best fit. The free parameters of the forward–reverse shock model and the two-component model are the input values of $\nu_{\rm m}$, $\nu_{\rm c}$, $\nu_{\rm a}$ and $f_{\rm m}$ at a given epoch, the jet-break time $t_{\rm j}$, electron index $p$ and the dust extinction $E(B-V)$ in the host galaxy. If the electron distribution is a hard power law, the synchrotron frequency $\nu_i$ corresponding to the upper cut-off of the distribution and an index $q$ parametrizing the time evolution of the cut-off will also be included as fit parameters (Resmi & Bhattacharya 2008). In the forward–reverse shock model, the spectral parameters of the reverse shock (RS) and the shock crossing time $t_{\rm x}$ are also included as free parameters. In the two-component model we have the deceleration time $t_{\rm dec}$ of the wide jet as an additional free parameter. Band-type smoothening is used in spectral (between multiple power laws of the synchrotron spectrum) and temporal (for a gradual transition of the spectral parameters across $t_{\rm j}$, $t_{\rm dec}$ and $t_{\rm x}$) domains (Granot & Sari 2002). We derive the physical parameters from the best-fitting spectral parameters. For the wind termination shock model, we use the afterglow code of Jóhannesson, Björnsson & Gudmundsson (2006) to calculate the light curves. It takes as input the physical parameters $E_{\rm iso}$, $A_*$, $\Delta n$, $R_{\rm sw}$, $p$, $\epsilon_{\rm e}$ and $\epsilon_{\rm b}$, where $\Delta n$ is the change in density at the wind termination shock and $R_{\rm sw}$ is the radius of the termination shock. In addition to these parameters, we also fit for dust extinction $A_V$ in the host frame. The multiwavelength fit therefore directly provides the best-fitting physical parameters. Note that, in this model, the definition of $\epsilon_{\rm e}$ has been changed from the one used in Jóhannesson et al. (2006) to that of Panaitescu & Kumar (2001b) to allow for values of $p < 2$.

### 3.1 Forward–reverse shocks

Shao & Dai (2005) modelled the *R*-band light curve alone using a forward–reverse shock model. In this model, for $T < 0.02$ d the RS dominates the emission. The rise at $T \sim 0.02$ d coincides with the passage of the synchrotron frequency of the FS through the *R* band, after which the FS dominates the light curve. However, in the *Swift V* band, with good sampling at $T < 0.02$ d, the light-curve decay is too shallow to be explained by standard RS emission. Nevertheless we first attempted a forward–reverse shock model where the optical light curve at $T < 0.02$ d is not entirely dominated by the RS, but also by the rising FS. This allowed us to have the steep decay of the RS, but still reproduce the early optical decay. However, this placed constraints on the temporal profile of the modelled FS emission at the early period. To reproduce the observed optical and X-ray light curves, we had to have a wind-driven density profile for the ambient medium, and a hard ($p < 2$) electron distribution (Bhattacharya 2001; Sagar et al. 2001; Misra et al. 2005; Resmi & Bhattacharya 2008) undergoing fast cooling during this time period. We do not have to include dust extinction in the host frame to achieve this fit. Along with further constraints on the FS emission from the later part of the optical and X-ray light curves, and the *Spitzer* spectrum (Heng et al. 2008) at 2.3 d, we narrowed down the parameter space. In Fig. 4, we present the best-fitting model (reduced chi squared, $\chi^2_{\rm DOF} = 3.9$ for a DOF of 223) along with the optical, X-ray and radio data. We obtained a good fit in the spectral parameter space, but the physical parameters inferred from these spectral fits turned out to be unrealistic (Table 3) and based on that we had to rule out this model.

### 3.2 Two-component outflow

We attempt a two-component model, where different outflows dominate the early- and late-time light curves. The most popular picture is of two co-aligned components with different opening angles (Berger et al. 2003; Racusin et al. 2008). For GRB 050525A, the first (narrow) jet dominates the emission at $T < 0.02$ d while the second (wide) jet gives rise to the *R*-band re-brightening at $T \sim 0.02$ d as it decelerates around this epoch, and dominates thereafter. The late-time optical and X-ray light curves are seen to steepen gradually. We assume this to be due to the lateral expansion of the wide component, and our best-fitting jet break is at $\sim$5 d. Due to the lack of dense sampling around this time, there are relatively larger uncertainties on this estimate. After $T > 0.1$ d the emission from the narrow component is required to decay faster so that the model does not overpredict the flux at later epochs. Even though various reasons could cause quenching, the most natural assumption is that the narrow component is undergoing lateral expansion around that time. The narrow jet contribution is significant in X-rays for sufficiently long time, and hence relatively good constraints on its $t_{\rm j}$ can be obtained from the X-ray light curve alone. A constant density ambient medium profile produced the best fit. The model required a Milky Way-type additional extinction in the host galaxy frame.

In Fig. 5, we present the best-fitting model along with the optical, X-ray and radio data. We obtain a somewhat high $\chi^2_{\rm DOF}$ of 4.5 (for a DOF of 223). Such large values are due to the small-scale fluctuations in the light curves, especially the scatter around the re-brightening epoch in the *R* band and the early flare-like feature in X-ray. Our best-fitting spectral and physical parameters are given in Table 4. Our fitting parameters (especially the value of $p$, the host extinction and $t_{\rm j}$ for the second jet) differ from the values reported in previous studies (Blustin et al. 2006; Della Valle et al. 2006; Heng et al. 2008), because our numerical code uses a more sophisticated description than the multiple power-law fitting employed in these papers. Since the narrow component is relevant only for a short period of time, its spectral parameters are not well constrained. We are only able to obtain lower limits to the self-absorption frequency ($\nu_{\rm a}$) and cooling frequency ($\nu_{\rm c}$). The inferred physical parameters are well within the range observed for other afterglows (Panaitescu & Kumar 2001a; Resmi & Bhattacharya 2008; Cenko et al. 2010). The ambient medium density is towards the higher end of what is normally estimated in afterglow modelling, leading to a wider inferred collimation angle for the given value of $t_{\rm j}$. The estimated value of kinetic energy in both the jets is similar. The initial Lorentz factor ($\Gamma_0$) of the wide jet is $\sim$10 and that of the narrow jet is $>$60, suggesting the more relativistic narrow jet to be responsible for the prompt gamma-ray emission. The energy in the narrow jet is $\sim$370 times that in the radiation observed by BAT ($2.3 \times 10^{52}$ erg, Blustin et al. 2006). This could indicate that only around 0.3 per cent of total energy is converted to radiation during the prompt emission phase, which is compatible with the low efficiencies expected for internal shocks (Daigne & Mochkovitch 1998). Since for both jets $\epsilon_{\rm e} \gg \epsilon_{\rm B}$, we estimated the expected inverse Compton emission and found it to be significantly lower than the synchrotron component.

The model agrees reasonably well with the VLA radio data in multiple frequencies; however, the radio light curves are more or less flat for the entire duration of VLA observation. The 8.4 and 4.8 GHz fluxes remain at the same level within error bars from 0.3 to 30 d. This could be caused either by contamination from the associated SN or by contribution from a nearby unresolved variable source (like an active galactic nucleus). We note that a similar flattening has been observed in other radio afterglows (Frail et al.

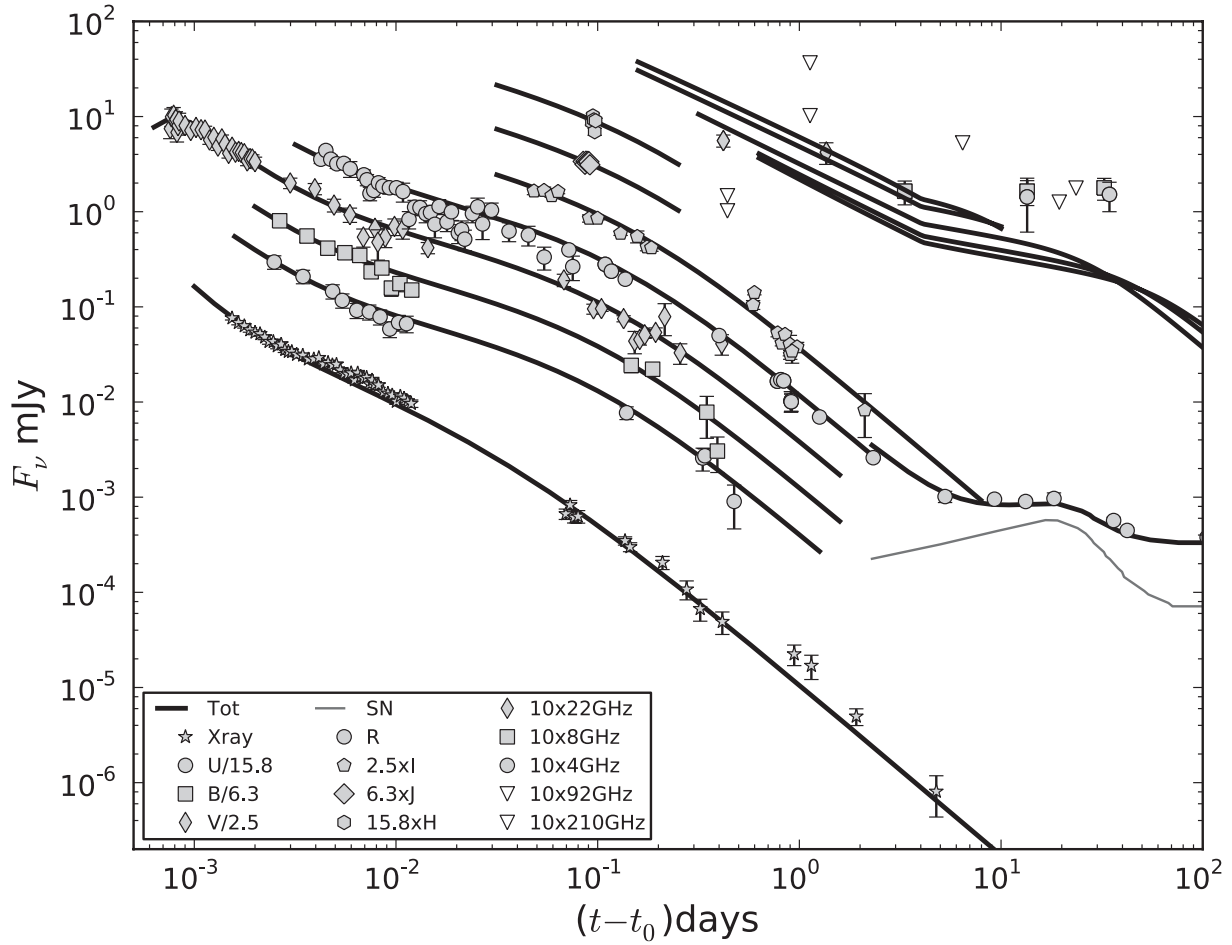


**Figure 4.** Optical *UBVRIJH*, *Swift* X-ray, radio and mm light curves of the afterglow of GRB 050525A along with the forward–reverse shock model. The SN component is shown as a thin grey line. The light curves are shifted arbitrarily for clarity. XRT data are recovered from Blustin et al. (2006) and the VLA radio data from the NRAO repository.

**Table 3.** Best-fitting ($\chi^2_{\rm DOF} \sim 3.9$) spectral and physical parameters of the forward–reverse shock model. No host extinction need to be used. However, the values of the derived physical parameters are unrealistic and hence we rule out this model.

| | | | | | | | |
|---|---|---|---|---|---|---|---|
| Shock | $\nu_{\rm a}$ (Hz) | $\nu_{\rm m}$ (Hz) | $\nu_{\rm c}$ (Hz) | $f_{\rm m}$ (mJy) | $p$ | $q$ | $t_{\rm j}$ (d) |
| | $\sim 10^{10}$ | $8.0^{+4.5}_{-5.5} \times 10^{15}$ | $7.08^{+5.5}_{-1.5} \times 10^{11}$ | $15.82^{+4.1}_{-1.72}$ | $1.82^{+0.08}_{-0.18}$ | $1.2 \pm 0.2$ | $0.04^{+0.01}_{-0.02}$ |
| Fwd. | $E_{\rm iso,52}$ (erg) | $A_*$ | $\epsilon_{\rm e}$ | $\epsilon_{\rm B}$ | $\theta_{\rm j}$ (°) | $E_{\rm tot,52}$ (erg) | – |
| | $11.75^{+0.21}_{-0.19}$ | $2.63^{+2.9}_{-0.71} \times 10^{-6}$ | $1.6^{+0.9}_{-0.7} \times 10^{-3} \left(\frac{\nu_i}{3\times10^{19}\,{\rm Hz}}\right)^{0.12}$ | $(2.5 \pm 1.8) \times 10^7$ | $0.11^{+0.03}_{-0.02}$ | $2.^{1.2}_{-0.7} \times 10^{-5}$ | – |
| Shock | $\nu_{\rm a}$ (Hz) | $\nu_{\rm m}$ (Hz) | $\nu_{\rm c}$ (Hz) | $f_{\rm m}$ (mJy) | $p$ | $t_{\rm x}$ (d) | |
| | – | $2.^{+2.}_{-0.74} \times 10^{11}$ | $2.95^{+2.94}_{-1.47} \times 10^{15}$ | $10.^{+1.2}_{-2.1}$ | $2.08 \pm 0.07$ | $7.9^{+1.}_{-0.86} \times 10^{-4}$ | |
| Rev. | – | – | $\epsilon_{\rm e}$ | $\epsilon_{\rm B}$ | $\Gamma_0$ | – | |
| | – | – | $\sim 1.1$ | $(1. \pm 0.2) \times 10^{-3}$ | $1073^{+116}_{-204}$ | – | |

2004). Nevertheless, we have provided the best possible fits to the available radio data within our model. The steepening in the light curves corresponds to the epoch when the fireball becomes optically thin to synchrotron radiation.

### 3.3 Wind-driven bubble and termination shock

The two-component model agrees well with the overall behaviour of the multiwavelength light curves. However, for the early X-ray light curve (0.001−0.012 d), only the average behaviour is explained by this model. The X-ray light curve during this period displays mild flares. In an attempt to explain this finer feature, we opted for another model where the ambient density profile changes shape, such as in a wind bubble. The immediate neighbourhood of the burst has a stratified density profile up to the termination shock $R_{\rm sw}$, where the afterglow shock encounters a density jump as well as a change in the density profile. When the FS enters the density enhancement it rapidly slows down and the comoving density of the shocked matter is increased. There is therefore an increased number of radiating electrons but their average energy is lower. This causes the afterglow temporal decay to be slower for $\nu < \nu_{\rm c}$ but faster

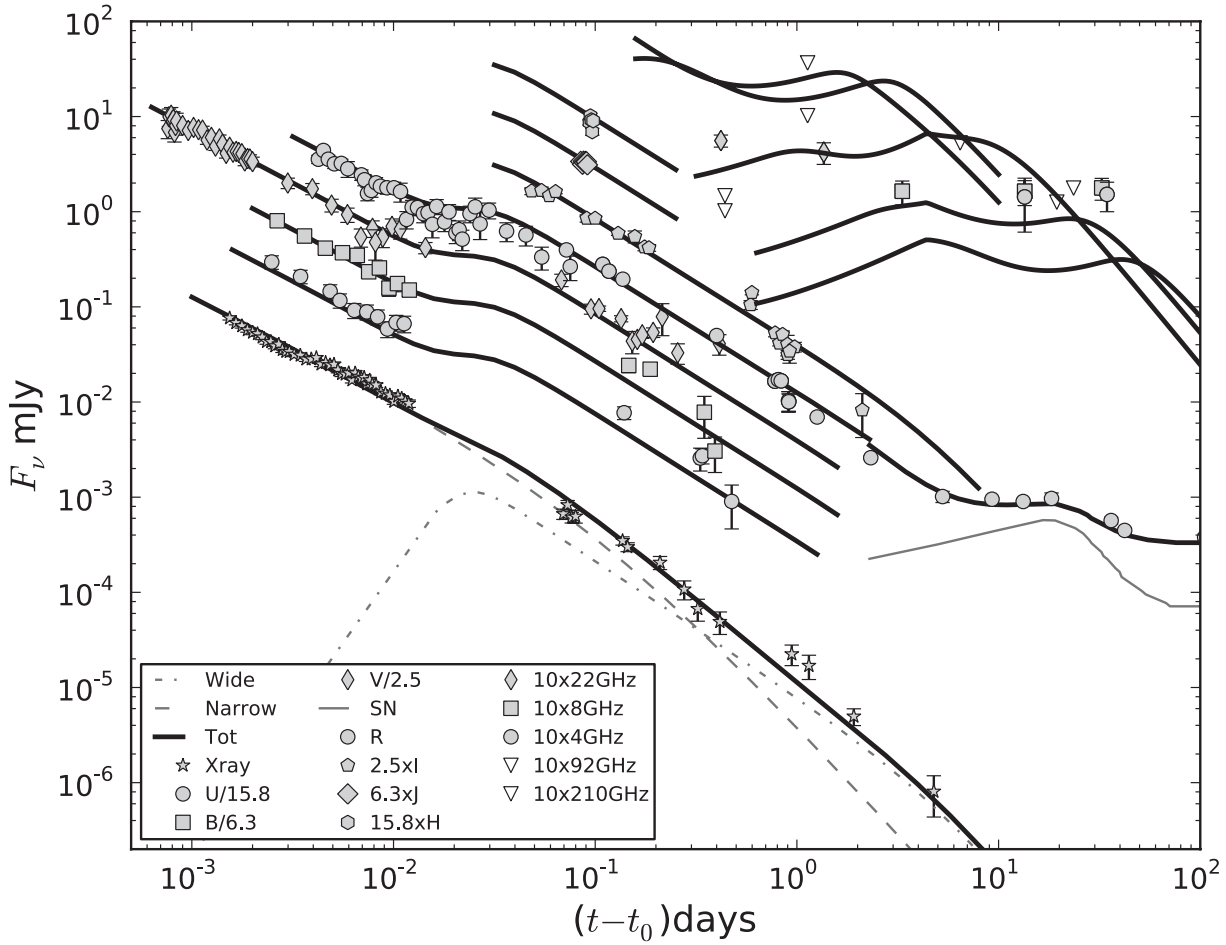


**Figure 5.** Same as in Fig. 4 but for the best-fitting two-component outflow model. For the X-ray light curve, the contribution from the narrow and wide components is shown as dashed and dash–dotted curves separately.

**Table 4.** Best-fitting spectral and physical parameters of the two-component outflow model. The best-fitting $A_v$ (host) is $0.16 \pm 0.06$ mag (Milky Way type). The spectral parameters are quoted at the jet-break time of the respective components. Variabilities in the early optical and X-ray light curves result in a large value of $\chi^2_{\rm DOF} \sim 4.5$.

| | | | | | | | |
|---|---|---|---|---|---|---|---|
| Component | $\nu_a$ (Hz) | $\nu_m$ (Hz) | $\nu_c$ (Hz) | $f_m$ (mJy) | $p$ | $t_j$ (d) | $t_{dec}$ (d) |
| Wide | $(4.6^{+0.1}_{-0.4}) \times 10^{10}$ | $(3.5^{+1.1}_{-0.8}) \times 10^{10}$ | $(4.0 \pm 3.0) \times 10^{16}$ | $2.23^{+2.6}_{-1.7}$ | $2.6 \pm 0.08$ | $5.0 \pm 3.0$ | 0.025 |
| | $E_{iso,52}$ (erg) | $n_0$ (atom cm$^{-3}$) | $\epsilon_e$ | $\epsilon_B$ | $\theta_j$ (°) | $E_{tot,52}$ (erg) | $\Gamma_0$ |
| Component | $9.35^{+10.3}_{-9.0}$ | $354.8^{267.7}_{-154.6}$ | $0.126 \pm 0.02$ | $(5.1 \pm 3.4) \times 10^{-5}$ | $(24.8^{+4.7}_{-0.7})$ | $0.43 \pm 0.25$ | $7.1 \pm 2.1$ |
| | $\nu_a$ (Hz) | $\nu_m$ (Hz) | $\nu_c$ (Hz) | $f_m$ (mJy) | $p$ | $t_j$ (d) | $t_{dec}$ (d) |
| Narrow | $>6.3 \times 10^{11}$ | $(1.0^{+1.1}_{-0.1}) \times 10^{11}$ | $>2.6 \times 10^{19}$ | $23.72^{+1.7}_{-2.6}$ | $2.37 \pm 0.02$ | $0.1^{+0.02}_{-0.01}$ | $>7.5 \times 10^{-4}$ |
| | $E_{iso,52}$ (erg) | $n_0$ (atom cm$^{-3}$) | $\epsilon_e$ | $\epsilon_B$ | $\theta_j$ (°) | $E_{tot,52}$ (erg) | $\Gamma_0$ |
| | $852.56 \left(\frac{\nu_c}{3\times10^{19}}\right)^{1/4}$ | 354.8 | $0.014 \left(\frac{\nu_c}{3\times10^{19}}\right)^{1/4}$ | $6.1 \times 10^{-6} \left(\frac{\nu_c}{3\times10^{19}}\right)^{-5/4}$ | <3.26 | $0.69 \left(\frac{\nu_c}{3\times10^{19}}\right)^{1/4}$ | >60 |

for $\nu > \nu_c$ because $\nu_c$ rapidly decreases when the shock enters the density jump (Jóhannesson 2006). The afterglow then settles into a power-law decay in the constant density medium. If $\nu_c$ remains between the optical and X-ray observing bands in this afterglow, this model can reproduce the optical bump observed in the light curve.

Our best-fitting model is shown in Fig. 6 where the wind termination shock is placed at ∼0.09 pc (corresponding to the observer frame time $T \sim 900$ s), and has a density increase of a factor of ∼12. The set of parameters used for the model are given in Table 5. The model parameters differ from those determined from the two-component model given in Table 4 because of the different

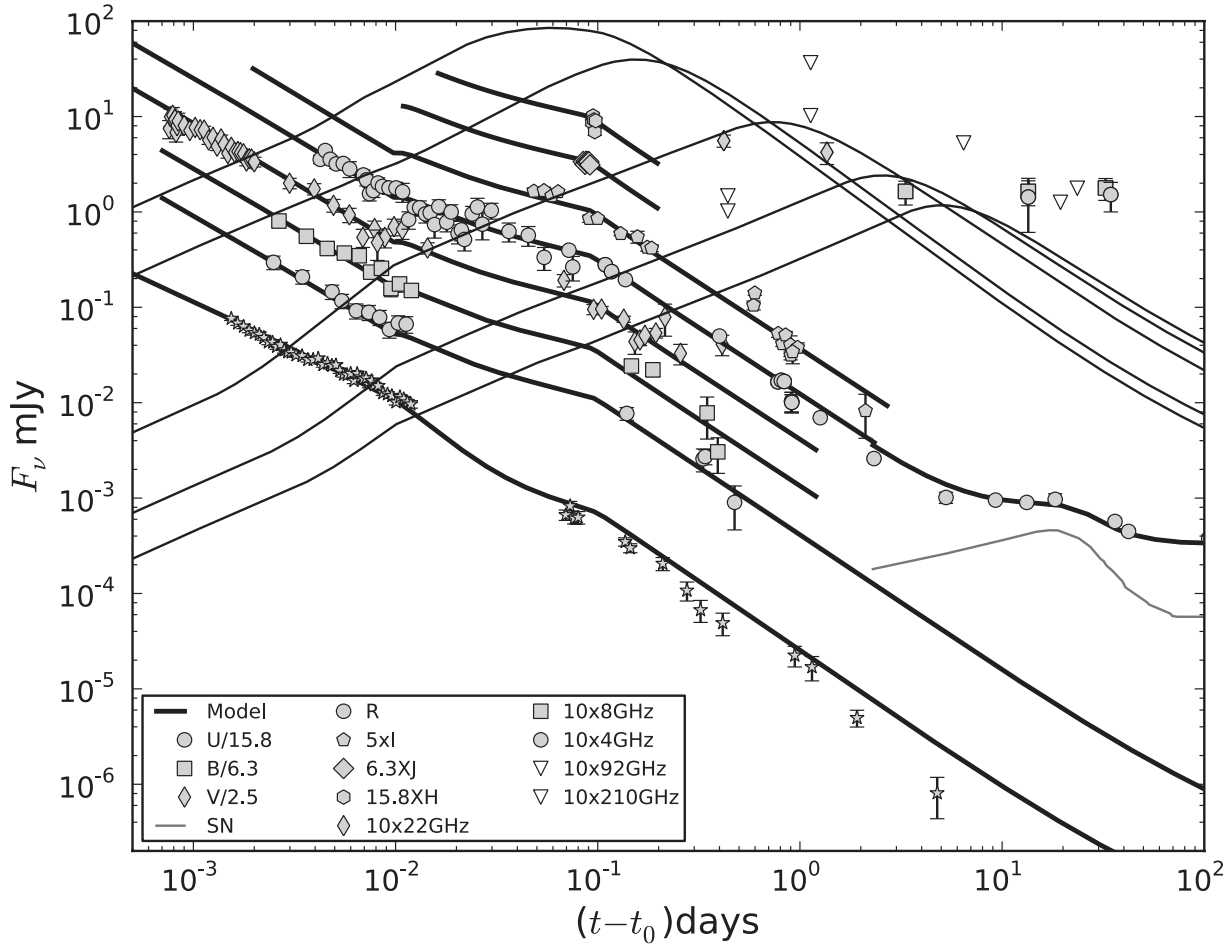


**Figure 6.** Same as in Fig. 5 but for the best-fitting wind termination shock model.

**Table 5.** Parameters of the wind termination shock model. For explanation of parameters see Jóhannesson et al. (2006). Note that the definition of $\epsilon_e$ has been changed to allow for values of $p < 2$ as in Panaitescu & Kumar (2001b). Values without uncertainties were fixed in the model and do not affect the results significantly. Dust extinction in the host frame is $A_v = 0.15 \pm 0.05$ (SMC type). The best-fitting model yields a $\chi^2_{DOF} \sim 3.6$.

| Parameter | Value |
|---|---|
| $E_{tot,52}$ (erg) | $0.1^{+0.9}_{-0.08}$ |
| $\theta_j$ (°) | $<1.1$ |
| $A_*$ | $0.5^{+10}_{-0.45}$ |
| $\Delta n^a$ | $>12$ |
| $R^b_{sw}$ (pc) | $0.09 \pm 0.06$ |
| $p$ | $1.85 \pm 0.15$ |
| $\epsilon_e/10^{-5}$ | $1^{+5}_{-0.9}$ |
| $\epsilon_B/10^{-4}$ | $3^{+9}_{-2.8}$ |

[a]Fractional change in density at the termination shock.
[b]Radius of the termination shock.

modelling approach. The parameters are more like the narrow component in the two-component model, in agreement with the fact that it better fits the early afterglow data than the late data. The typical distance to a Wolf–Rayet (WR) star termination shock ranges from ∼0.1 pc to a few hundred pc depending on the mass-loss rate of the star and the interstellar medium surrounding it (Eldridge et al. 2006; van Marle et al. 2006; Eldridge 2007b). The radius of the wind termination shock is much smaller than that expected for a typical WR star, possibly indicating that the afterglow erupted from the rotational axis and the star was in a dense interstellar environment (Eldridge 2007a).

While the model adequately describes the optical and IR light curves and early X-ray light curve, it overpredicts the late-time X-ray light curve and underpredicts the late-time radio observations. A possible explanation for this difference is a change in the shock physics causing the cooling break frequency to decrease further, for example a small increase in the magnetic field strength of the shock. Further density fluctuations might also explain the differences as numerical modelling have shown the wind of massive stars to be more structured than we assume in our model (Eldridge 2007a). We obtain a $\chi^2_{DOF}$ of ∼3.6 (for a DOF of 223). For this model too, the scatter in the *R* band around the re-brightening epoch contributes to the somewhat large value of $\chi^2$.

### 3.4 Supernova contribution

Optical light curves of several low-redshift GRBs show a late-time red bump (Zeh, Klose & Hartmann 2004), often attributed to the emission from an SN believed to be associated with the progenitor of the GRB (Heger et al. 2003). Around $T \sim 5$ d, a flattening of the

*R*-band light curve was observed for GRB 050525A (Della Valle et al. 2006) with a temporal profile similar to the 'SN bump' seen in other afterglows. The late-time (∼36 d) VLT spectrum observed by Della Valle et al. also showed similarities to the spectra of other GRB-associated SNe. We compared the late-time *R*-band light curve with the prototypical SN98bw (Galama et al. 1998), the first known example of an SN associated with a GRB. We used the template optical light curves of SN98bw (Galama et al. 1998), *k*-corrected for the redshift of GRB 050525A. Best agreement with the observed *R*-band data for $T > 5$ d was obtained after shifting the SN98bw template by $-0.9$ d and applying a temporal stretch factor of 0.8. We did not have to adjust the magnitude of the shifted SN98bw, implying the associated SN to be of similar brightness as SN98bw. The host galaxy *R*-band magnitude was fixed at 25.1 (Della Valle et al. 2006). The SN component is shown as thin grey lines in Figs 4–6.

## 4 SUMMARY

We have presented the optical afterglow of GRB 050525A in *VRIJH* photometric bands. Our data fill some gaps in the optical multiwavelength light curves beyond 0.01 d and provide a better constraint on the optical decay index. Our IR observations, though confined to a narrow time bin, provide additional spectral constraints. The mm upper limits contributes to a better picture of the low-frequency behaviour of the afterglow.

We have undertaken a comprehensive multiwavelength modelling of the afterglow and tested various models against the data. The afterglow behaviour is too complex for a simple blast-wave model. We find that including emission from a possible RS component is not sufficient to explain the afterglow evolution. Either the outflow is structured as a two-component jet or the ambient medium has a complex structure involving a variation in the density profile. Our two-component jet model is able to reproduce the overall behaviour of the afterglow, except the finer fluctuation in the early X-ray light curve. The wind termination shock model succeeds in explaining the early phase including the short time-scale features but deviates from the late-time data. The radio light curves are moderately well explained by both models. Afterglow modelling is necessary to unravel the nature of the outflow and the structure of the medium around the burst. The complexity of the observed light curves demands that the most realistic models are used. Dense sampling and long monitoring campaigns are also required in conjunction with afterglow modelling.

## ACKNOWLEDGMENTS

We are thankful to an anonymous referee for useful comments and suggestions which has improved the presentation of the paper. We also thank and acknowledge the observing support at different observatories in collecting the data. This research has made use of data obtained through the High Energy Astrophysics Science Archive. We thank the VLA staff for easy access to the archival data base. The National Radio Astronomy Observatory is a facility of the National Science Foundation operated under cooperative agreement by Associated Universities Inc. Research Center Online Service, provided by the NASA/Goddard Space Flight Center. This work contains observations carried out with the IRAM PdBI. IRAM is supported by INSU/CNRS (France), MPG (Germany) and IGN (Spain). We thank the support of the Spanish MICINN projects AYA2009-14000-C03-01 and AYA2008-03467/ESP. The DARK Cosmology Center is funded by the DNRF.

## REFERENCES

Band D. et al., 2005, GCN, 3466, 1
Berger E. et al., 2003, Nat, 426, 154
Bhattacharya D., 2001, Bull. Astron. Soc. India, 29, 107
Blustin A. J. et al., 2006, ApJ, 637, 901
Calzetti D., 1997, AJ, 113, 162
Cameron P. B., Frail D. A., 2005, GCN, 3495, 1
Cardelli J. A., Clayton G. C., Mathis J. S., 1989, ApJ, 345, 245
Cenko S. B. et al., 2010, ApJ, 711, 641
Chevalier R. A., Li Z.-Y., 1999, ApJ, 520, L29
Chincarini G. et al., 2007, ApJ, 671, 1903
Daigne F., Mochkovitch R., 1998, MNRAS, 296, 275
Della Valle M. et al., 2006, ApJ, 642, L103
Eldridge J. J., 2007a, MNRAS, 377, L29
Eldridge J. J., 2007b, Phil. Trans. R. Soc., 365, 1255
Eldridge J. J., Genet F., Daigne F., Mochkovitch R., 2006, MNRAS, 367, 186
Foley R. J., Chen H., Bloom J., Prochaska J. X., 2005, GCN, 3483, 1
Frail D. A., Metzger B. D., Berger E., Kulkarni S. R., Yost S. A., 2004, ApJ, 600, 828
Galama T. J. et al., 1998, Nat, 395, 670
Gehrels N. et al., 2004, ApJ, 611, 1005
Granot J., Sari R., 2002, ApJ, 568, 820
Guilloteau S. et al., 1992, A&A, 262, 624
Heger A., Fryer C. L., Woosley S. E., Langer N., Hartmann D. H., 2003, ApJ, 591, 288
Henden A., 2005, GCN, 3855, 1
Heng K., Lazzati D., Perna R., Garnavich P., Noriega-Crespo A., Bersier D., Matheson T., Pahre M., 2008, ApJ, 681, 1116
Jóhannesson G., 2006, PhD thesis, Univ. Iceland
Jóhannesson G., Björnsson G., Gudmundsson E. H., 2006, ApJ, 647, 1238
Klotz A., Boër M., Atteia J. L., Stratta G., Behrend R., Malacrino F., Damerdji Y., 2005, A&A, 439, L35
Liang E.-W., Racusin J. L., Zhang B., Zhang B.-B., Burrows D. N., 2008, ApJ, 675, 528
Mészáros P., Rees M. J., 1999, MNRAS, 306, L39
Misra K., Resmi L., Pandey S. B., Bhattacharya D., Sagar R., 2005, Bull. Astron. Soc. India, 33, 487
Nousek J. A. et al., 2006, ApJ, 642, 389
Paczynski B., Rhoads J. E., 1993, ApJ, 418, L5
Panaitescu A., Kumar P., 2001a, ApJ, 560, L49
Panaitescu A., Kumar P., 2001b, ApJ, 554, 667
Pe'er A., Wijers R. A. M. J., 2006, ApJ, 643, 1036
Pei Y. C., 1992, ApJ, 395, 130
Piran T., 1999, Phys. Rep., 314, 575
Racusin J. L. et al., 2008, Nat, 455, 183
Rees M. J., Meszaros P., 1992, MNRAS, 258, 41P
Resmi L., Bhattacharya D., 2008, MNRAS, 388, 144
Rhoads J. E., 1999, ApJ, 525, 737
Sagar R. et al., 2001, Bull. Astron. Soc. India, 29, 91
Shao L., Dai Z. G., 2005, ApJ, 633, 1027
Stetson P. B., 1987, PASP, 99, 191
van Marle A. J., Langer N., Achterberg A., García-Segura G., 2006, A&A, 460, 105
Wijers R. A. M. J., Galama T. J., 1999, ApJ, 523, 177
Zeh A., Klose S., Hartmann D. H., 2004, ApJ, 609, 952
Zhang B., Fan Y. Z., Dyks J., Kobayashi S., Mészáros P., Burrows D. N., Nousek J. A., Gehrels N., 2006, ApJ, 642, 354

This paper has been typeset from a TEX/LATEX file prepared by the author.